

## Supporting Information

Generation of a Mn(IV)–Peroxo or Mn(III)–Oxo–Mn(III) Species upon Oxygenation  
of Mono- and Binuclear Thiolate-Ligated Mn(II) Complexes

Chien-Ming Lee<sup>\*,†</sup>, Wun-Yan Wu,<sup>†</sup> Ming-Hsi Chiang,<sup>\*,‡</sup> D. Scott Bohle<sup>\*,§</sup>  
and Gene-Hsiang Lee<sup>⊥</sup>

<sup>†</sup>Department of Applied Science, National Taitung University, Taitung 950,  
Taiwan

<sup>‡</sup>Institute of Chemistry, Academia Sinica, Taipei 115, Taiwan

<sup>§</sup>Department of Chemistry, McGill University, Montreal, Quebec H3A 0B8,  
Canada

<sup>⊥</sup>Instrumentation Center, National Taiwan University, Taipei 107, Taiwan

## Contents

**Figure S1.** The change of absorbance at 535 nm responsible for [PPN][Mn<sup>II</sup>(<sup>TMS</sup>PS3)(DABCO)](**2**) upon addition of different equivalents of DABCO into the solution of [PPN]<sub>2</sub>[(Mn<sup>II</sup>(<sup>TMS</sup>PS3))<sub>2</sub>] (**1**; 0.3 mM).

**Figure S2.** Magnetic susceptibility plots of  $\chi_M$  (open circles) and  $\chi_M T$  (open squares) *versus* temperature for **4**. The solid line is the best fit of the experimental data to the theoretical expression.

**Figure S3.** Comparison of cyclic voltammograms of Li<sub>3</sub><sup>TMS</sup>PS3 (black line), **1** (red line) and **2** (blue line) measured in a 1 mM CH<sub>3</sub>CN solution with 0.1 M [*n*-Bu<sub>4</sub>N][PF<sub>6</sub>] as the supporting electrolyte at room temperature, scan rate 0.1 V/s.

**Figure S4.** The 77 K EPR X-band spectra for **1** (orange; 0.6 mM) and **2** (purple; 0.6 mM) frozen in CH<sub>3</sub>CN. The experimental parameters: microwave frequency = 9.54 GHz, microwave power = 5 mW, modulation amplitude = 1.6 G.

**Figure S5.** ESI-MS spectra of **1** in CH<sub>3</sub>CN. Some oxygenated fragments may be derived from oxygenation during the injection of solution of **1** into the instrument. Simulations for some major fragments are also presented.<sup>1</sup>

**Figure S6.** Black line shows the UV–vis spectrum of [PPN]<sub>2</sub>[(Mn<sup>III</sup>(<sup>TMS</sup>PS3))<sub>2</sub>( $\mu$ -O)] (**4**) generated from the reaction of [PPN]<sub>2</sub>[(Mn<sup>II</sup>(<sup>TMS</sup>PS3))<sub>2</sub>](**1**) (0.098 mM) and [PPN][Mn<sup>IV</sup>(O<sub>2</sub>)(<sup>TMS</sup>PS3)](**3**) (0.065 mM) based on eq :  $3/2 \mathbf{1} + \mathbf{3} \rightarrow 2 \mathbf{4}$ . Red line shows the UV–vis spectrum of **4** generated from reaction of [PPN][Mn<sup>II</sup>(<sup>TMS</sup>PS3)(DABCO)] (**2**) (0.195 mM) and **3** (0.065 mM) based on eq :  $3 \mathbf{2} + \mathbf{3} \rightarrow 2 \mathbf{4}$ .

**Figure S7.** Microcrystals of **2** were placed under dry O<sub>2</sub> at ambient temperature for 30 min. (a) Microcrystals of **2** appears to be a light-purple color. (b) The color change during oxidation of solid-state **2** with O<sub>2</sub> is observed from light purple to dark red-purple.

**Figure S8.** (a) Conversion of **2** to **3** monitored by ATR-FTIR spectroscopy after microcrystals of **2** were stood in open air at ambient temperature. The initial spectrum is labeled as black solid line. The measured interval between two curves is 3 min. (b) FTIR spectra of solid-state **2** upon treating <sup>16</sup>O<sub>2</sub> (red line) and <sup>18</sup>O<sub>2</sub> (black line). (c) a

difference spectrum between FTIR spectra of solid-state **2** upon treating  $^{16}\text{O}_2$  and  $^{18}\text{O}_2$ .

**Figure S9.** The powder diffraction patterns of microcrystal **2** after exposed to  $\text{O}_2$  for 2 h (black solid line) and microcrystal **3** (red line, acting as a standard). The powder X-ray diffraction (PXRD) data were performed at the wiggler beamline BL17A at National Synchrotron Radiation Research Center (NSRRC), Taiwan. The experimental wavelength of the X-ray source is 1.3216 Å. Silicon powder was used as the calibrant and the refined sample-to-detector distance is 251 mm. Samples were ground firstly and packed into a 1.0 mm glass capillary and measured at room temperature.

**Figure S10.** Black line shows the UV-vis spectrum obtained from reaction of  $[\text{PPN}][\text{Mn}^{\text{II}}(\text{TMSPS3})(\text{DABCO})]$  (**2**) (0.2 mM) and excess amounts  $\text{O}_2$  (purging into the solution) in  $\text{CH}_3\text{CN}$  at ambient temperature. UV-vis spectra of  $[\text{PPN}]_2[\text{Mn}^{\text{III}}(\text{TMSPS3})_2(\mu\text{-O})]$  (**4**) (8%, red line) and  $[\text{PPN}][\text{Mn}^{\text{IV}}(\text{O}_2)(\text{TMSPS3})]$  (**3**) (63 %, blue line) are calculated for best fit to the experiment data (black line).

**Figure S11.** Black line shows the UV-vis spectrum obtained from reaction of  $[\text{PPN}][\text{Mn}^{\text{II}}(\text{TMSPS3})(\text{DABCO})]$  (**2**) (0.2 mM) and excess amounts  $\text{O}_2$  (layered above the solution) in  $\text{CH}_3\text{CN}$  at ambient temperature. UV-vis spectra of  $[\text{PPN}]_2[\text{Mn}^{\text{III}}(\text{TMSPS3})_2(\mu\text{-O})]$  (**4**) (25 %, red line) and  $[\text{PPN}][\text{Mn}^{\text{IV}}(\text{O}_2)(\text{TMSPS3})]$  (**3**) (37 %, blue line) are calculated for the best fit with experiment data (black line).

**Figure S12.** Changes in UV-vis spectra (gray lines) after treating **2** (black line) with excess amounts of  $\text{O}_2$  in  $\text{CH}_3\text{CH}_2\text{CN}$  at  $-80^\circ\text{C}$ . Red line represent the UV-vis spectrum of Mn(IV)-peroxo **3**. The time interval is 2 min.

**Figure S13.** Changes of infrared spectra monitored by ATR-FTIR spectroscopy after microcrystals of **1** were stood in open air at ambient temperature. The initial spectrum is labeled as black solid line. The measured interval between two curves is 5 min.

**Figure S14.** Microcrystals of **1** were placed under dry  $\text{O}_2$  at ambient temperature for 2 h. (a) Microcrystals of **1** appears to be an orange-red color. (b) The color change during oxidation of solid-state **1** with  $\text{O}_2$  is observed from orange red to yellow brown.

**Figure S15.** (a) Black line shows the UV-vis spectrum obtained from reaction of

[PPN]<sub>2</sub>[(Mn<sup>II</sup>(<sup>TMS</sup>PS3))<sub>2</sub>](**1**) (0.16 mM) and excess amounts O<sub>2</sub> (purging into the solution) in CH<sub>3</sub>CN at ambient temperature. UV–vis spectra of [PPN]<sub>2</sub>[(Mn<sup>III</sup>(<sup>TMS</sup>PS3))<sub>2</sub>(μ-O)] (**4**) (50 %, red line) and [PPN][Mn<sup>IV</sup>(O<sub>2</sub>)(<sup>TMS</sup>PS3)](**3**) (24 %, blue line) are calculated for the best fit with experiment data (black line). (b) Black line shows the UV–vis spectrum obtained from reaction of [PPN]<sub>2</sub>[(Mn<sup>II</sup>(<sup>TMS</sup>PS3))<sub>2</sub>](**1**) (0.16 mM) and excess amounts O<sub>2</sub> (layered above the solution) in CH<sub>3</sub>CN at ambient temperature. UV–vis spectra of [PPN]<sub>2</sub>[(Mn<sup>III</sup>(<sup>TMS</sup>PS3))<sub>2</sub>(μ-O)] (**4**) (68 %, red line) and [PPN][Mn<sup>IV</sup>(O<sub>2</sub>)(<sup>TMS</sup>PS3)](**3**) (12 %, blue line) are calculated for best fitting with experiment data (black line).

**Figure S16.** (a) Oxidation of **2** (one equiv.) with ferrocenium tetrafluoroborate (one equiv, [Fc][BF<sub>4</sub>]) under N<sub>2</sub> leads to the formation of mononuclear neutral Mn(III) [Mn(<sup>TMS</sup>PS3)(DABCO)] (yield, 90%). (b) Comparisons of UV–vis spectra between **2** (black line, 0.2 mM in CH<sub>3</sub>CN) and [Mn<sup>III</sup>(<sup>TMS</sup>PS3)(DABCO)] (red line, 0.2 mM in THF). (c) ORTEP diagrams of neutral [Mn<sup>III</sup>(<sup>TMS</sup>PS3)(DABCO)] with thermal ellipsoids drawn at the 50% probability level (X-ray Crystallographic Data shown in Table S1). Hydrogen atoms and solvent of crystallization are omitted for clarity. (d) Selected bond distances (Å) and angles (deg) of **2** and [Mn<sup>III</sup>(<sup>TMS</sup>PS3)(DABCO)].

**Figure S17.** ESI-MS spectra of **2** in CH<sub>3</sub>CN (negative mode). The oxygenated fragments may be derived from oxygenation with air during the injection of solution of **2** into the instrument.

**Figure S18** (a) UV–vis spectra of **1** (0.50 mM) in CH<sub>3</sub>CN measured at variant temperature. (b) UV–vis spectra of **1** (0.50 mM) with DABCO (100 equiv) (suggesting 100 % conversion from **1** to **2**) in CH<sub>3</sub>CN measured at variant temperature.

**Figure S19.** Optimized *ab initio* gas phase structure of the 3-proton S = 5/2 analog of the DABCO anion **2**. Density function theory, B3LYP/6-31+g\*, with a double zeta basis set used.

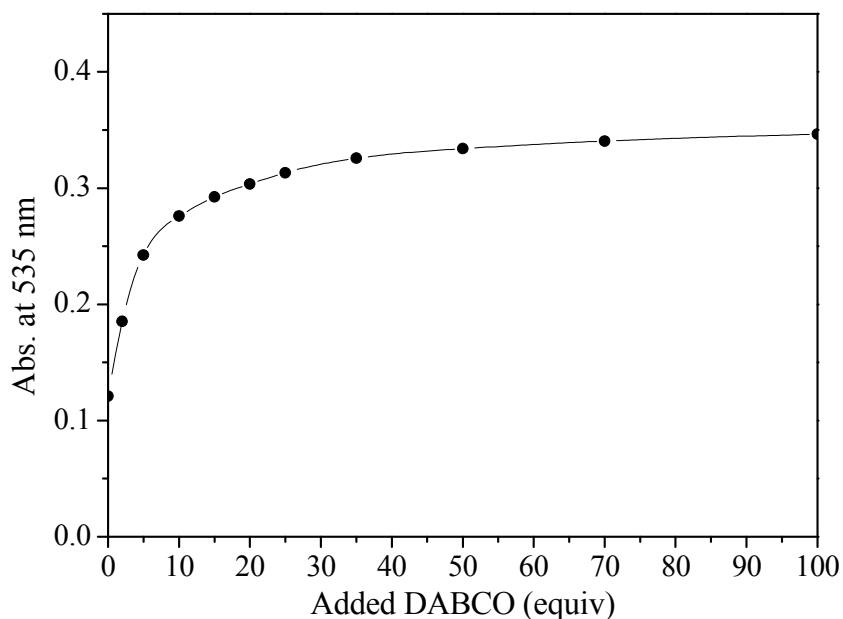
**Table S1.** X-ray Crystallographic Data for **1**, **2**, **4** and [Mn<sup>III</sup>(<sup>TMS</sup>PS3)(DABCO)]

**Table S2.** Contrast in calculated and experimental ground states for **2** for two spin states

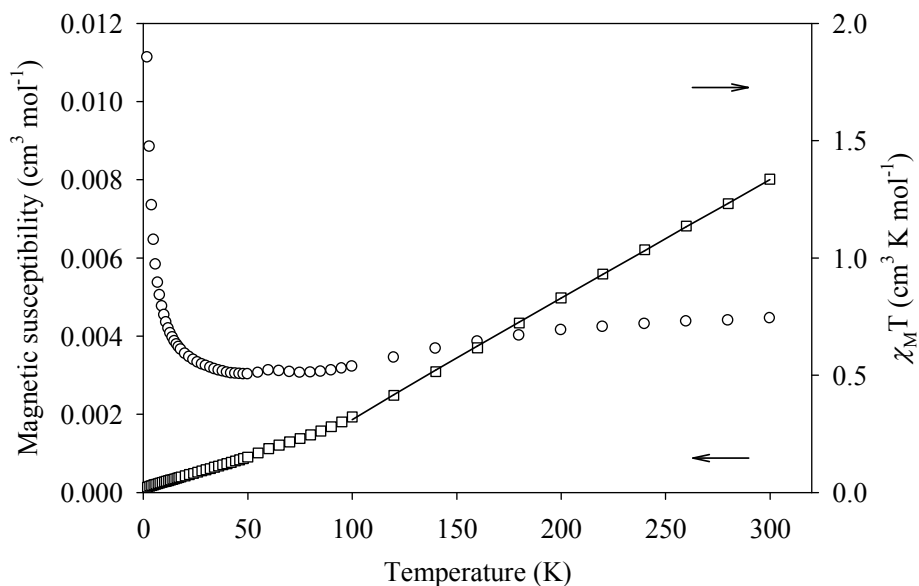
**Table S3.** Electronic Spectra Data Calculated with DFT-TD for **2** in nm (with intensity given as oscillator strength)

## **Computational Details**

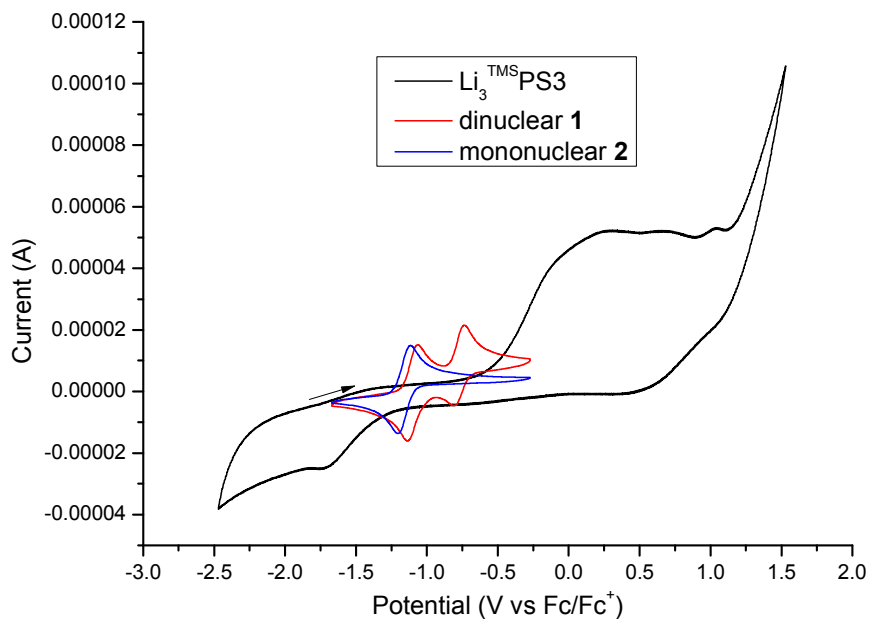
## **References**



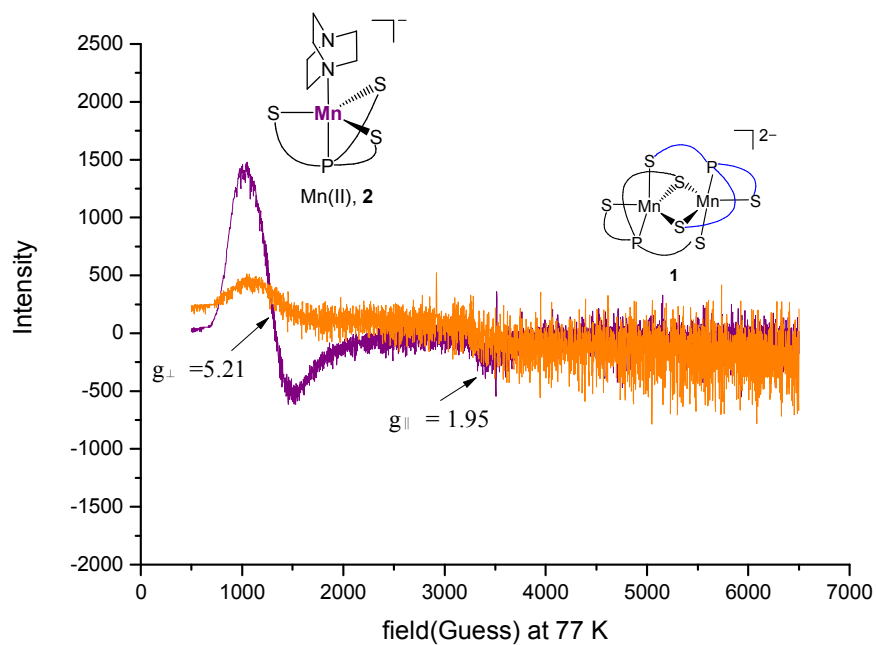
**Figure S1.** The change of absorbance at 535 nm responsible for  $[\text{PPN}][\text{Mn}^{\text{II}}(\text{TMS}^{\text{PS3}})(\text{DABCO})](\mathbf{2})$  upon addition of different equivalents of DABCO into the solution of  $[\text{PPN}]_2[(\text{Mn}^{\text{II}}(\text{TMS}^{\text{PS3}}))_2](\mathbf{1}; 0.3 \text{ mM})$ .



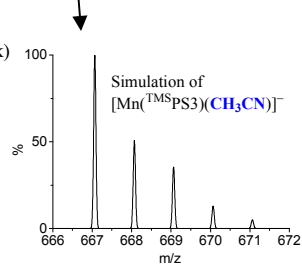
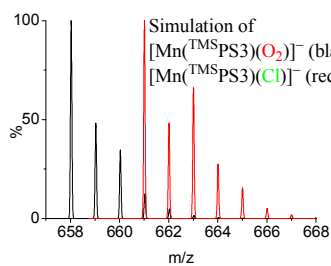
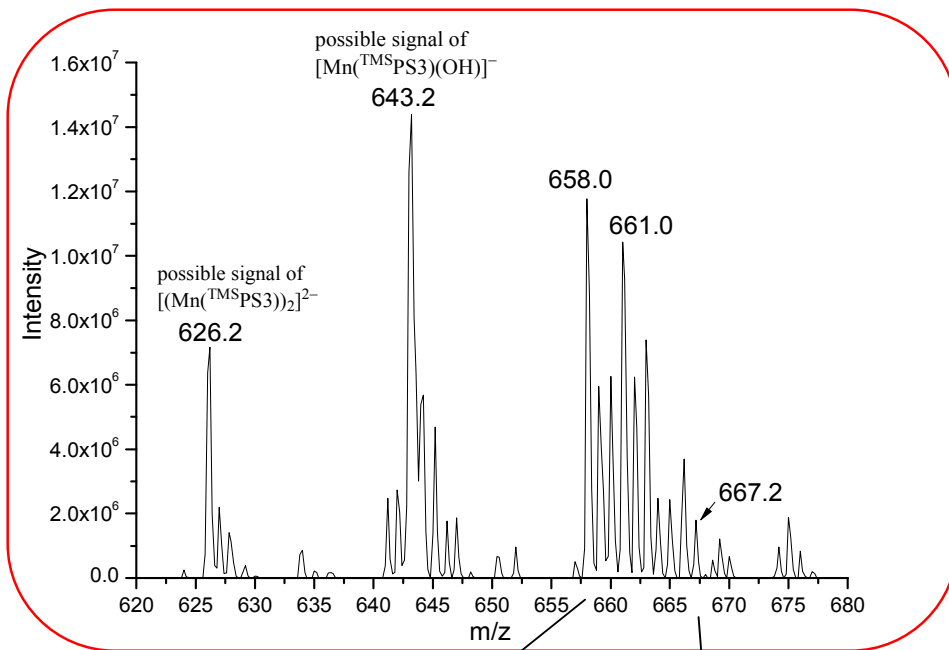
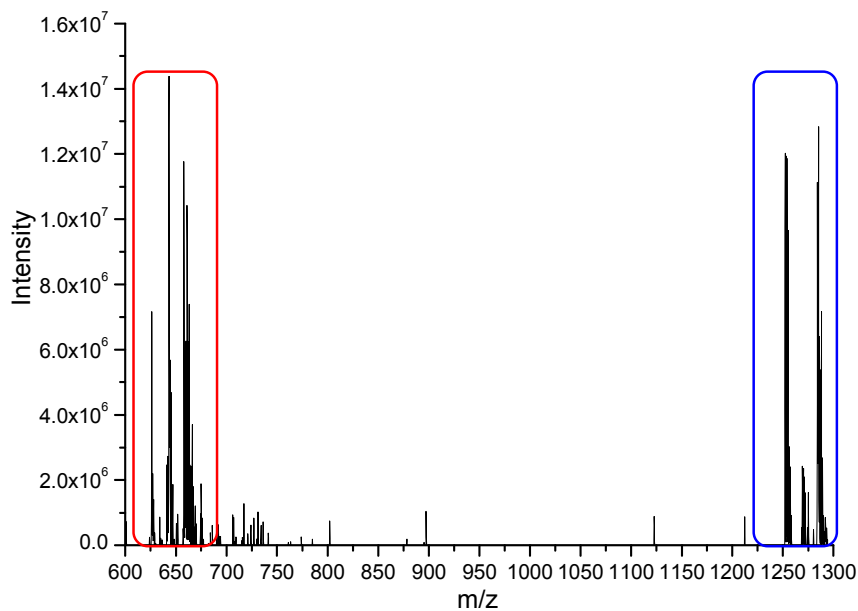
**Figure S2.** Magnetic susceptibility plots of  $\chi_M$  (open circles) and  $\chi_M T$  (open squares) versus temperature for **4**. The solid line is the best fit of the experimental data to the theoretical expression.



**Figure S3.** Comparison of cyclic voltammograms of  $\text{Li}_3^{\text{TMS}}\text{PS3}$  (black line), **1** (red line) and **2** (blue line) measured in a 1 mM  $\text{CH}_3\text{CN}$  solution with 0.1 M  $[\text{n-Bu}_4\text{N}][\text{PF}_6]$  as the supporting electrolyte at room temperature, scan rate 0.1 V/s.



**Figure S4.** The 77 K EPR X-band spectra for **1** (orange; 0.6 mM) and **2** (purple; 0.6 mM) frozen in  $\text{CH}_3\text{CN}$ . The experimental parameters: microwave frequency = 9.54 GHz, microwave power = 5 mW, modulation amplitude = 1.6 G.



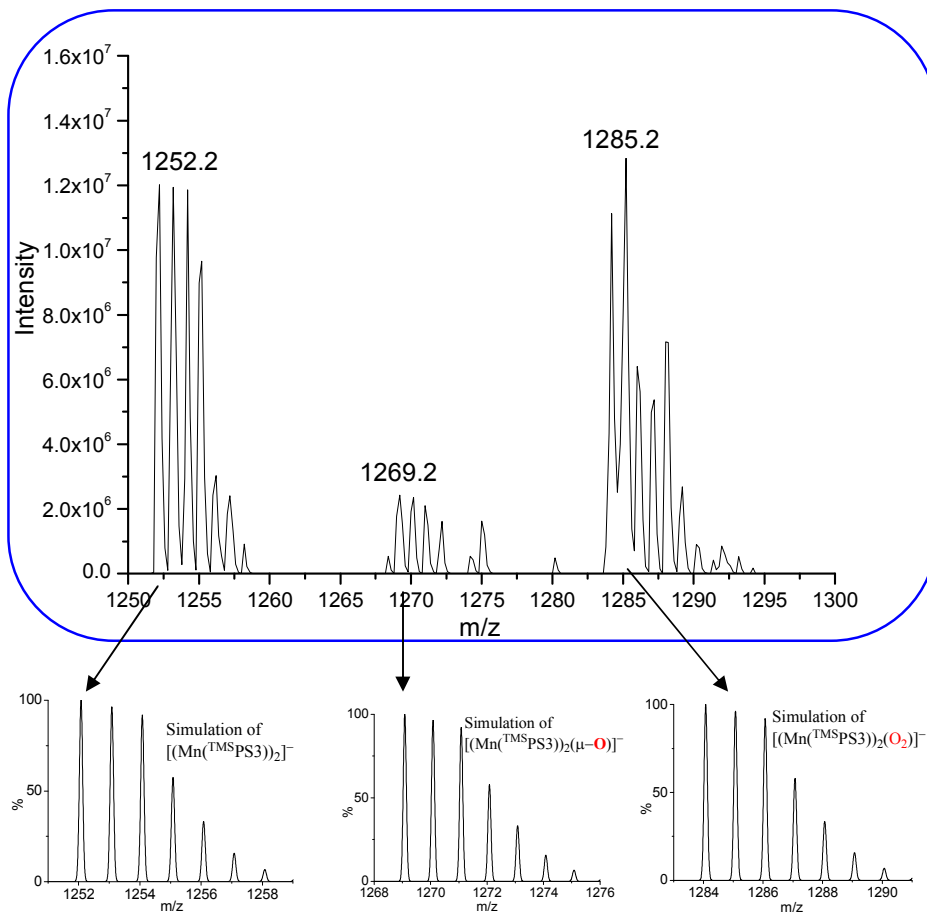


**Figure S5.** ESI-MS spectra of **1** in  $\text{CH}_3\text{CN}$  (negative mode). Some oxygenated fragments may be derived from oxygenation with air during the injection of solution of **1** into the instrument. Simulations for some major fragments are also presented.<sup>1</sup>

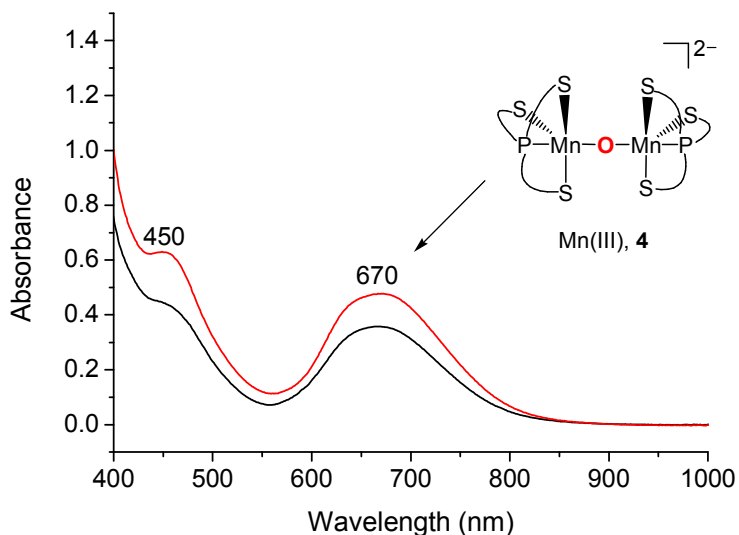


**Figure S6.** Black line shows the UV-vis spectrum of  $[\text{PPN}]_2[(\text{Mn}^{\text{III}}(\text{TMSPS3}))_2(\mu\text{-O})]$  (**4**) generated from the reaction of  $[\text{PPN}]_2[(\text{Mn}^{\text{II}}(\text{TMSPS3}))_2]$  (**1**) (0.098 mM) and  $[\text{PPN}][\text{Mn}^{\text{IV}}(\text{O}_2)(\text{TMSPS3})]$  (**3**) (0.065 mM) based on eq :  $3/2 \mathbf{1} + \mathbf{3} \rightarrow 2 \mathbf{4}$ . Red line shows the UV-vis spectrum of **4** generated from reaction of  $[\text{PPN}][\text{Mn}^{\text{II}}(\text{TMSPS3})\text{-}(\text{DABCO})]$  (**2**) (0.195 mM) and **3** (0.065 mM) based on eq :  $3 \mathbf{2} + \mathbf{3} \rightarrow 2 \mathbf{4} + 3 \text{DABCO}$ .

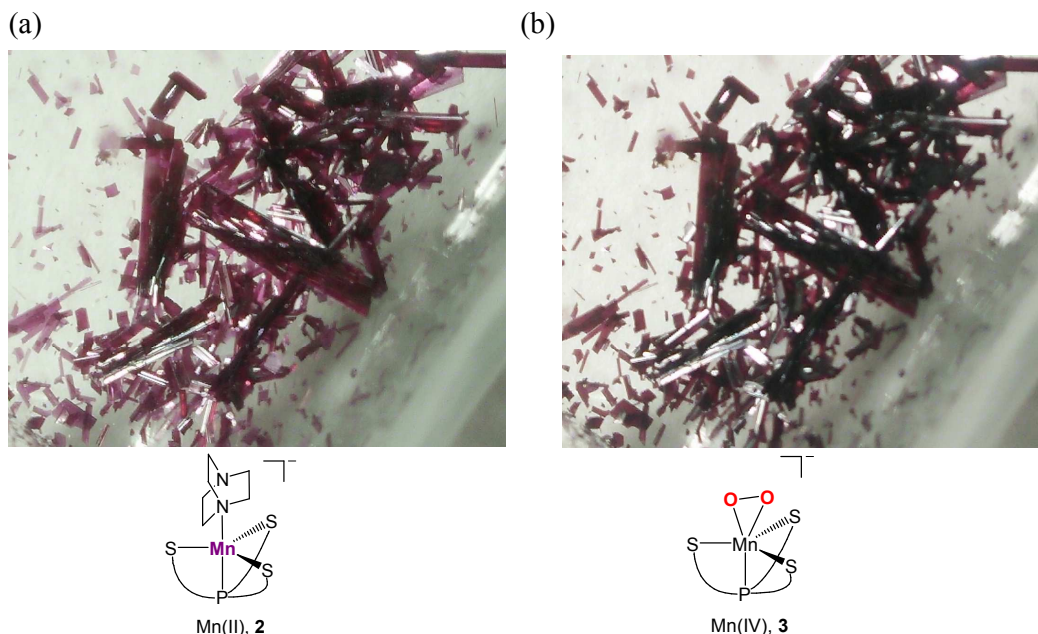


**Figure S7.** Microcrystals of **2** were placed under dry  $\text{O}_2$  at ambient temperature for 30 min. (a) Microcrystals of **2** appears to be a light-purple color. (b) The color change during oxidation of solid-state **2** with  $\text{O}_2$  is observed from light purple to dark red-purple.

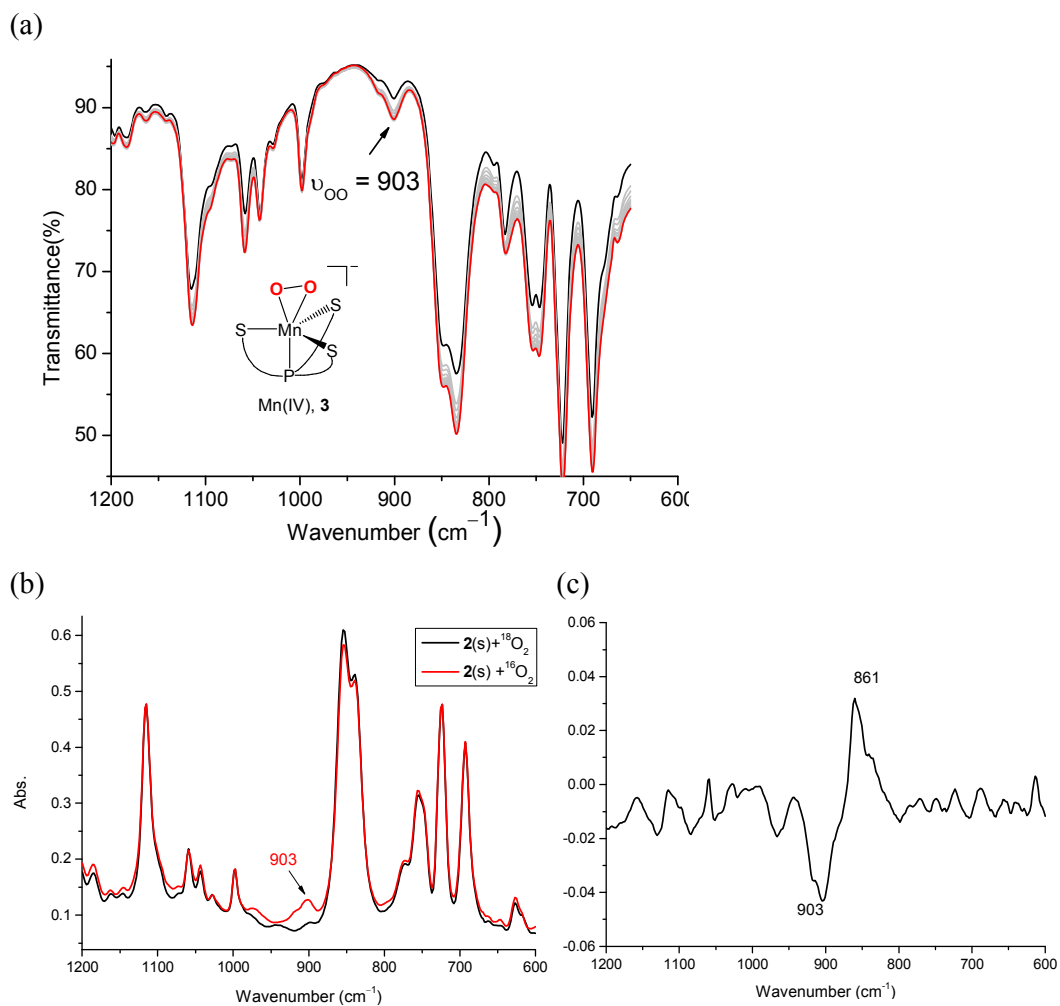


**Figure S8.** (a) Conversion of **2** to **3** monitored by ATR-FTIR spectroscopy after microcrystals of **2** were stood in open air at ambient temperature. The initial spectrum is labeled as black solid line. The measured interval between two curves is 3 min. (b) FTIR spectra of solid-state **2** upon treating  $^{16}\text{O}_2$  (red line) and  $^{18}\text{O}_2$  (black line). (c) a difference spectrum between FTIR spectra of solid-state **2** upon treating  $^{16}\text{O}_2$  and  $^{18}\text{O}_2$ .

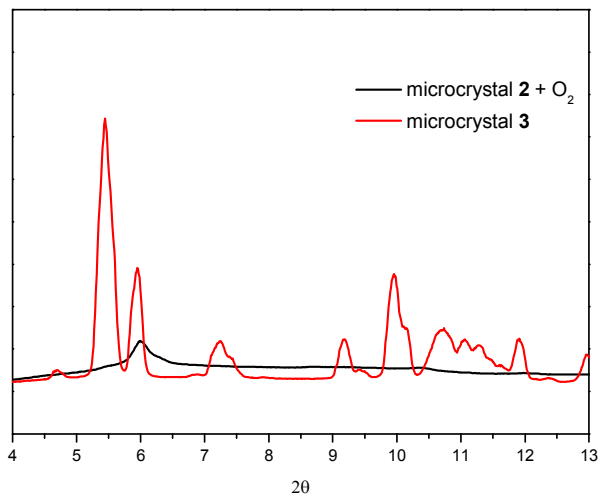


**Figure S9.** The powder diffraction patterns of microcrystal **2** after exposed to O<sub>2</sub> for 2 h (black solid line) and microcrystal **3** (red line, acting as a standard). The powder X-ray diffraction (PXRD) data were performed at the wiggler beamline BL17A at National Synchrotron Radiation Research Center (NSRRC), Taiwan. The experimental wavelength of the X-ray source is 1.3216 Å. Silicon powder was used as the calibrant and the refined sample-to-detector distance is 251 mm. Samples were ground firstly and packed into a 1.0 mm glass capillary and measured at room temperature.

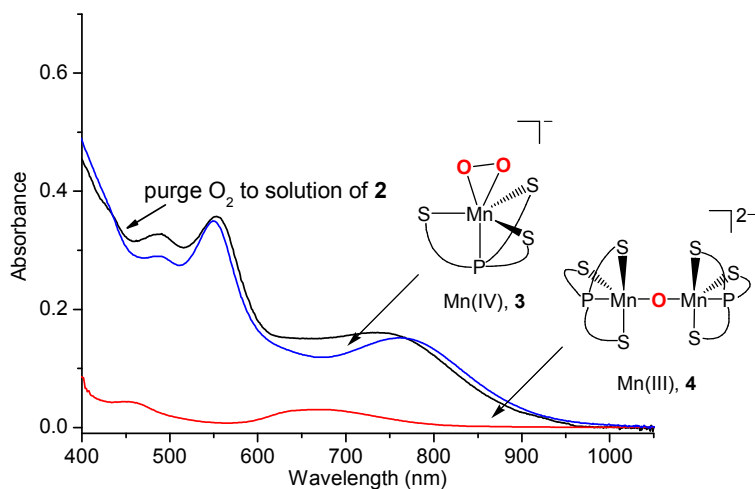


**Figure S10.** Black line shows the UV-vis spectrum obtained from reaction of [PPN][Mn<sup>II</sup>(<sup>TMS</sup>PS3)(DABCO)] (**2**) (0.2 mM) and excess amounts O<sub>2</sub> (purging into the solution) in CH<sub>3</sub>CN at ambient temperature. UV-vis spectra of [PPN]<sub>2</sub>[(Mn<sup>III</sup>(<sup>TMS</sup>PS3))<sub>2</sub>(μ-O)] (**4**) (8%, red line) and [PPN][Mn<sup>IV</sup>(O<sub>2</sub>)(<sup>TMS</sup>PS3)](**3**) (63 %, blue line) are calculated for best fit to the experiment data (black line).

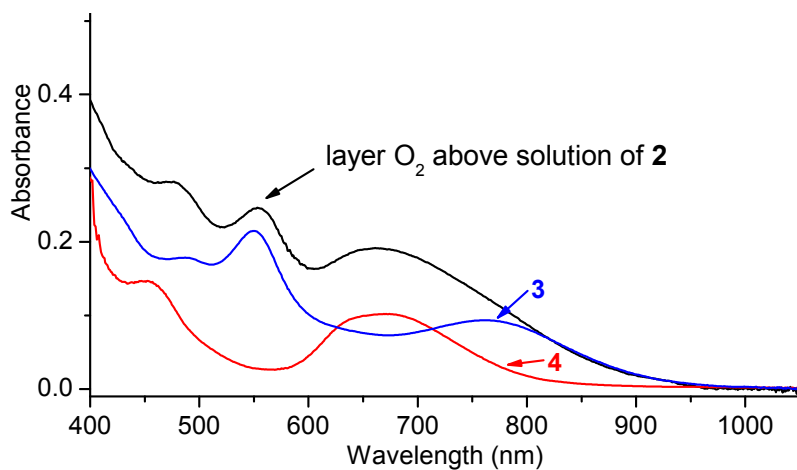


**Figure S11.** Black line shows the UV-vis spectrum obtained from reaction of  $[\text{PPN}][\text{Mn}^{\text{II}}(\text{TMSPS3})(\text{DABCO})]$  (**2**) (0.2 mM) and excess amounts  $\text{O}_2$  (layered above the solution) in  $\text{CH}_3\text{CN}$  at ambient temperature. UV-vis spectra of  $[\text{PPN}]_2[\text{Mn}^{\text{III}}(\text{TMSPS3})_2(\mu\text{-O})]$  (**4**) (25 %, red line) and  $[\text{PPN}][\text{Mn}^{\text{IV}}(\text{O}_2)(\text{TMSPS3})]$  (**3**) (37 %, blue line) are calculated for the best fit with experiment data (black line).

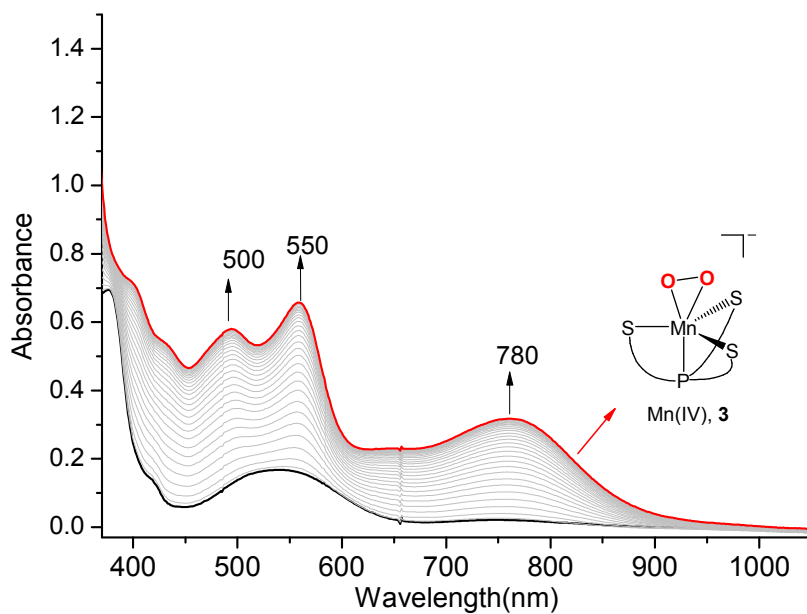


**Figure S12.** Changes in UV-vis spectra (gray lines) after treating **2** (black line) with excess amounts of  $\text{O}_2$  in  $\text{CH}_3\text{CH}_2\text{CN}$  at  $-80^\circ\text{C}$ . Red line represent the UV-vis spectrum of Mn(IV)-peroxo **3**. The time interval is 2 min.

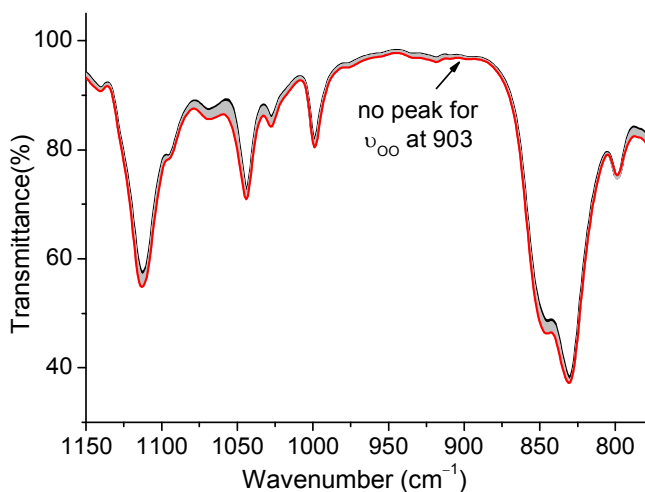


**Figure S13.** Changes of infrared spectra monitored by ATR-FTIR spectroscopy after microcrystals of **1** were stood in open air at ambient temperature. The initial spectrum is labeled as black solid line. The measured interval between two curves is 5 min.

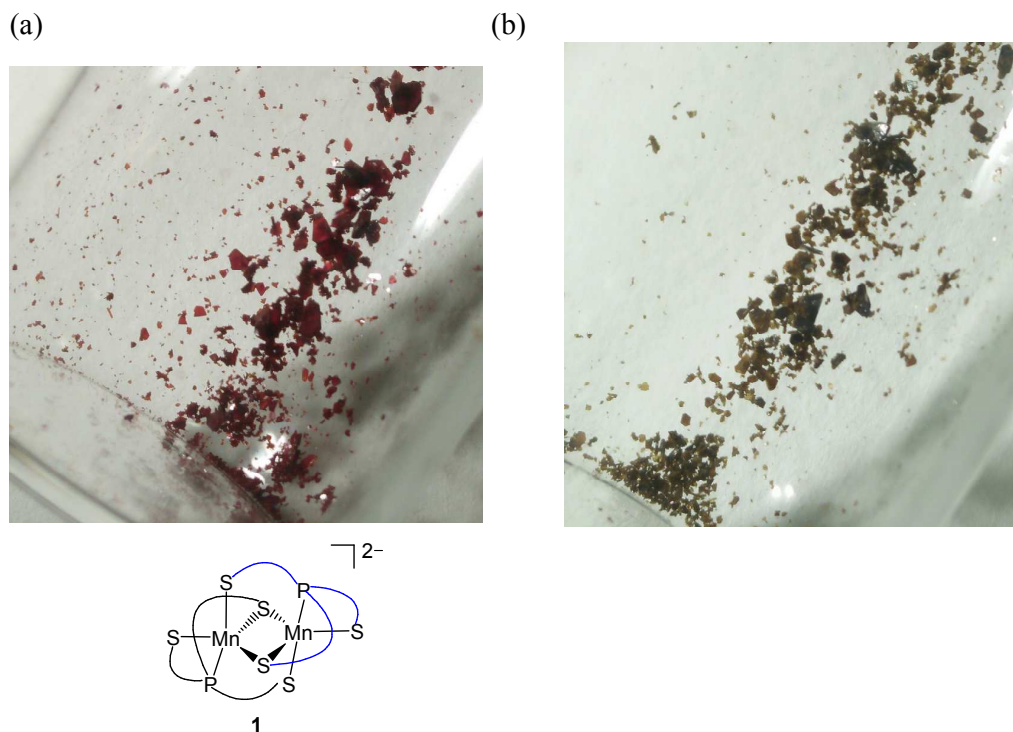


**Figure S14.** Microcrystals of **1** were placed under dry O<sub>2</sub> at ambient temperature for 2 h. (a) Microcrystals of **1** appears to be an orange-red color. (b) The color change during oxidation of solid-state **1** with O<sub>2</sub> is observed from orange red to yellow brown.

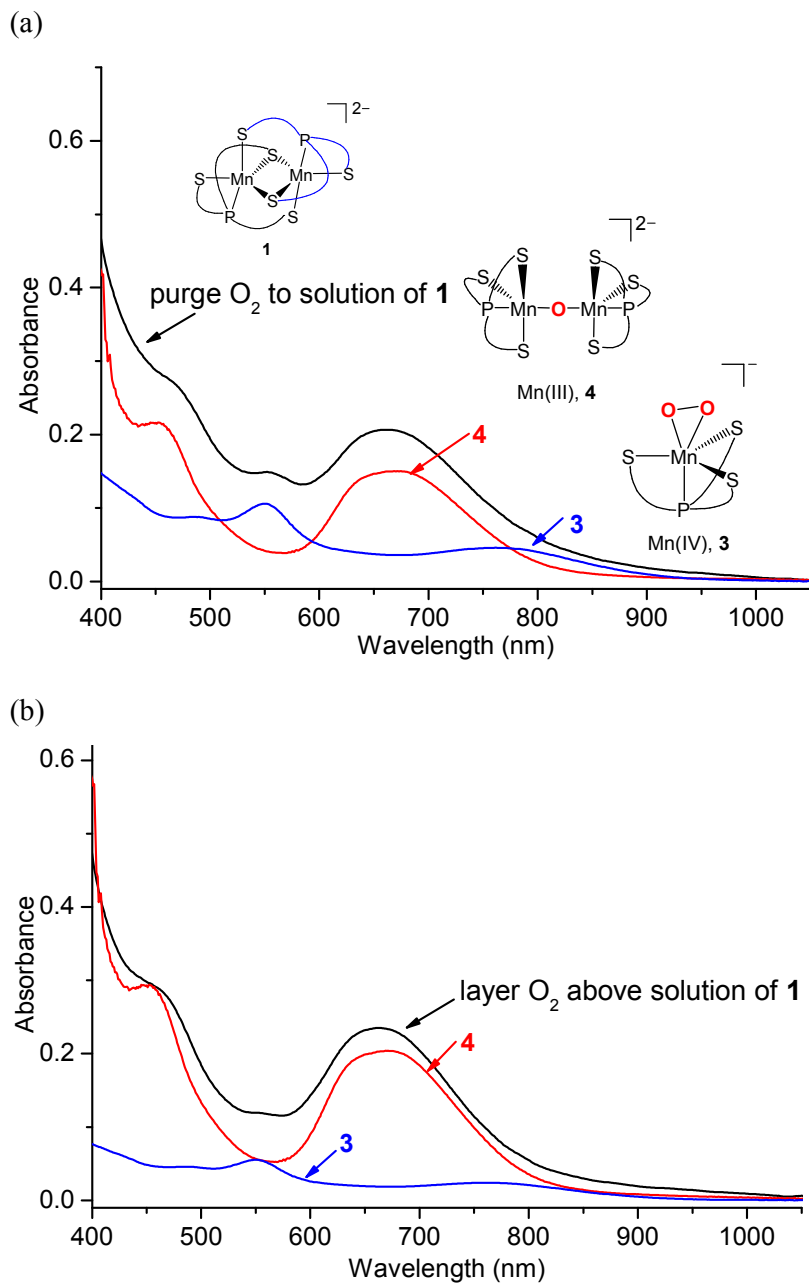


**Figure S15.** (a) Black line shows the UV-vis spectrum obtained from reaction of  $[\text{PPN}]_2[\text{Mn}^{\text{II}}(\text{TMS}^{\text{PS}}\text{S}_3)_2]$  (**1**) (0.16 mM) and excess amounts  $\text{O}_2$  (purging into the solution) in  $\text{CH}_3\text{CN}$  at ambient temperature. UV-vis spectra of  $[\text{PPN}]_2[\text{Mn}^{\text{III}}(\text{TMS}^{\text{PS}}\text{S}_3)_2(\mu\text{-O})]$  (**4**) (50 %, red line) and  $[\text{PPN}][\text{Mn}^{\text{IV}}(\text{O}_2)(\text{TMS}^{\text{PS}}\text{S}_3)]$  (**3**) (24 %, blue line) are calculated for the best fit with experiment data (black line). (b) Black line shows the UV-vis spectrum obtained from reaction of  $[\text{PPN}]_2[\text{Mn}^{\text{II}}(\text{TMS}^{\text{PS}}\text{S}_3)_2]$  (**1**) (0.16 mM) and excess amounts  $\text{O}_2$  (layered above the solution) in  $\text{CH}_3\text{CN}$  at ambient temperature. UV-vis spectra of  $[\text{PPN}]_2[\text{Mn}^{\text{III}}(\text{TMS}^{\text{PS}}\text{S}_3)_2(\mu\text{-O})]$  (**4**) (68 %, red line) and  $[\text{PPN}][\text{Mn}^{\text{IV}}(\text{O}_2)(\text{TMS}^{\text{PS}}\text{S}_3)]$  (**3**) (12 %, blue line) are calculated for best fitting with experiment data (black line).

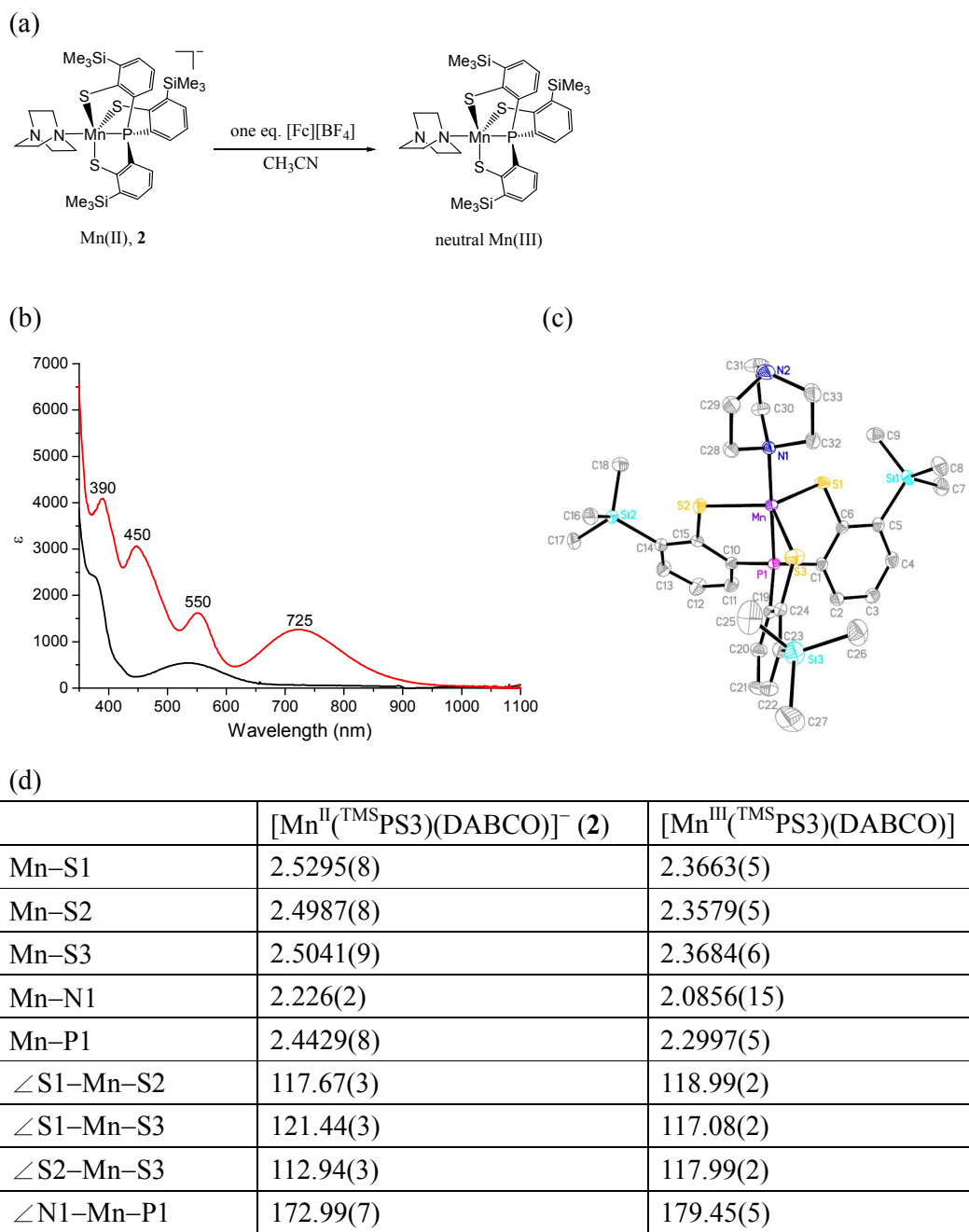


**Figure S16.** (a) Oxidation of **2** (one equiv.) with ferrocenium tetrafluoroborate (one equiv,  $[\text{Fc}][\text{BF}_4]$ ) under  $\text{N}_2$  leads to the formation of mononuclear neutral Mn(III)  $[\text{Mn}^{\text{III}}(\text{TMS}^3\text{PS}_3)(\text{DABCO})]$  (yield, 90%). (b) Comparisons of UV–vis spectra between **2** (black line, 0.2 mM in  $\text{CH}_3\text{CN}$ ) and  $[\text{Mn}^{\text{III}}(\text{TMS}^3\text{PS}_3)(\text{DABCO})]$  (red line, 0.2 mM in THF). (c) ORTEP diagrams of neutral  $[\text{Mn}^{\text{III}}(\text{TMS}^3\text{PS}_3)(\text{DABCO})]$  with thermal ellipsoids drawn at the 50% probability level (X-ray Crystallographic Data shown in Table S1). Hydrogen atoms and solvent of crystallization are omitted for clarity. (d) Selected bond distances ( $\text{\AA}$ ) and angles (deg) of **2** and  $[\text{Mn}^{\text{III}}(\text{TMS}^3\text{PS}_3)(\text{DABCO})]$ .

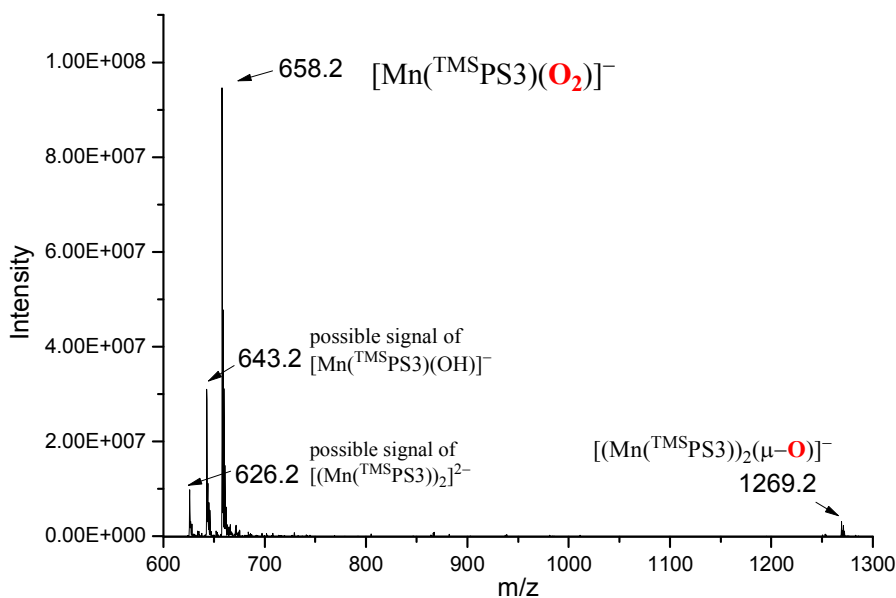


**Figure S17.** ESI-MS spectra of **2** in CH<sub>3</sub>CN (negative mode). The oxygenated fragments may be derived from oxygenation with air during the injection of solution of **2** into the instrument.

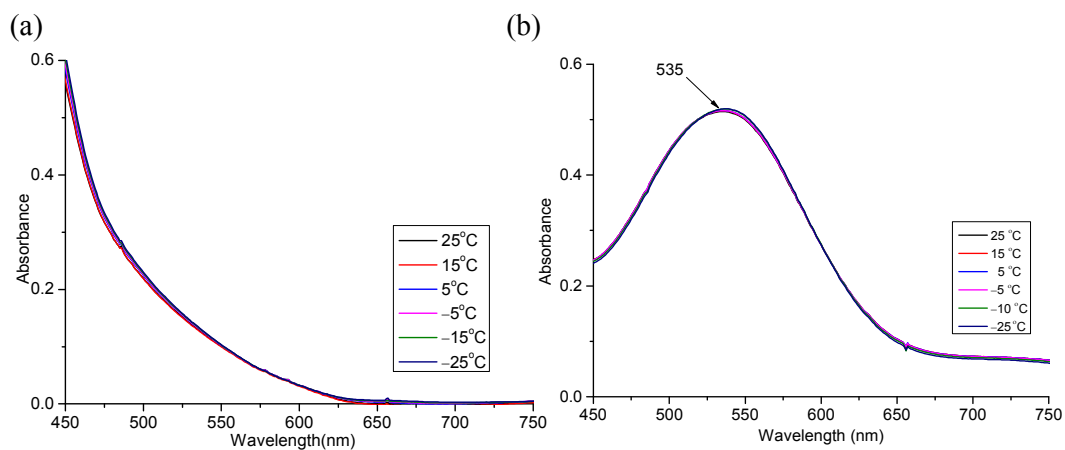


**Figure S18.** (a) UV-vis spectra of **1** (0.50 mM) in CH<sub>3</sub>CN measured at variant temperature. (b) UV-vis spectra of **1** (0.50 mM) with DABCO (100 equiv) (suggesting 100 % conversion from **1** to **2**) in CH<sub>3</sub>CN measured at variant temperature.

**Table S1.** X-ray Crystallographic Data for **1**, **2**, **4** and [Mn<sup>III</sup>(<sup>TMS</sup>PS3)(DABCO)]

	1·6THF	2·CH <sub>3</sub> CN	4·1.5ether·3.5C H <sub>3</sub> CN	[Mn <sup>III</sup> ( <sup>TMS</sup> PS3)( DABCO)]·THF
Empirical formula	C <sub>150</sub> H <sub>184</sub> Mn <sub>2</sub> N <sub>2</sub> O <sub>6</sub> P <sub>6</sub> S <sub>6</sub> Si <sub>6</sub>	C <sub>71</sub> H <sub>81</sub> Mn N <sub>4</sub> P <sub>3</sub> S <sub>3</sub> Si <sub>3</sub>	C <sub>139</sub> H <sub>157.5</sub> Mn <sub>2</sub> N <sub>5.5</sub> O <sub>2.5</sub> P <sub>6</sub> S <sub>6</sub> Si <sub>6</sub>	C <sub>37</sub> H <sub>56</sub> Mn N <sub>2</sub> O P S <sub>3</sub> Si <sub>3</sub>
Formula weight	2767.59	1318.69	2601.80	811.19
<i>T</i> , K	200(2) K	150(2)	150(2)	150(2)
Crystal system	Orthorhombic	Orthorhombic	Triclinic	Monoclinic
Space group	Pbca	Pna2 <sub>1</sub>	P-1	P2 <sub>1</sub> /c
<i>a</i> , Å	26.4554(7)	25.2754(10)	14.9573(6)	15.0330(4)
<i>b</i> , Å	20.2956(5)	9.8216(4)	16.8240(7)	11.8932(3)
<i>c</i> , Å	27.6687(8)	28.4013(10)	31.5766(12)	23.2927(7)
<i>α</i> , °	90	90	75.113(2)	90
<i>β</i> , °	90	90	82.277(2)	93.0579(9)
<i>γ</i> , °	90	90	68.066(2)	90
<i>V</i> , Å <sup>3</sup>	14856.1(7)	7050.5(5)	7116.9(5)	4158.6(2)
<i>Z</i>	4	4	2	4
$\rho_{\text{calcd}}$ , Mg m <sup>-3</sup>	1.237	1.242	1.214	1.296
$\mu$ , mm <sup>-1</sup>	0.421	0.438	0.434	0.624
Goodness-of-fit on F <sup>2</sup>	1.174	1.010	1.069	1.060
R [ <i>I</i> >2σ( <i>I</i> )] : R1 <sup>a</sup> (wR2) <sup>b</sup>	0.0772 (0.1726)	0.0303 (0.0651)	0.0830 (0.2025)	0.0340 (0.0832)
R (all data): R1 <sup>a</sup> (wR2) b	0.1022(0.1850)	0.0377 (0.0679)	0.1571 (0.2448)	0.0430 (0.0900)

$$^a R1 = (\sum||F_o|-|F_c||)/(\sum|F_o|). \quad ^b wR2 = [\sum w(F_o^2 - F_c^2)^2 / \sum w(F_o^2)^2]^{1/2}.$$

## Computational Details

**ab initio calculations.** To better understand the electronic structure and nature of the intermediates in these reactions *ab initio* density functional theory has been employed to model the ground states and their spectroscopy. For computational efficiency the model adopted had the three trimethylsilyl groups truncated to three protons, Figure S17. Both high and low spin ground states were optimized and both ground state structures are contrasted with the solid state crystallographic data in Table S2.

**Table S2.** Contrast in calculated and experimental ground states for **2** for two spin states

Metric	S = 5/2	S = 1/2	Exp.
Energy	-3725.579	-3725.535	-
(A.U.)	32749	93600	-
Mn-N	2.31181 Å	2.20397 Å	2.226(2) Å
Mn-P	2.44523	2.19397	2.4429(8)
Mn-S	2.54017	2.32156	2.5695(8)
Mn-S	2.53976	2.30806	2.4987(8)
Mn-S	2.53986	2.33250	2.5041(9)
S-Mn-S	117.87°	112.96°	117.67(3)°
S-Mn-S	118.07	132.02	121.44(3)
S-Mn-S	117.69	113.77	112.94(3)

As can be seen the contraction of the coordination sphere predicted with a low spin state is not in agreement with the experimental data which is well described by the high spin geometry. Over all the metric parameters for the truncated ligand used in the calculated model are quite close to those found for experimental chelate ligand.

Surprisingly the DABCO ligand has an experimental Mn–N bond length about 0.09 Å closer than the calculated value and yet the steric constraints for the model complex are expected to be less due to the truncation of the three trimethylsilyl groups. This indicates that in the condensed phase of the crystal structure packing effects, in particular the presence of the PPN cation, are important.

The predicted high spin ground state for **2** is consistent with the observed spectroscopy. The gas phase electronic energy difference for the anion, gives 27.2 kcal/mol in favor of the high spin state. This is clearly in accord with the magnetic results and also the room temperature electronic spectra calculated for the first 30 states by time dependent DFT, Table S3.

As can be seen in Table S3 the first observed visible band at 535 nm corresponds well with the lowest energy band in for the high spin spectrum, but there is a marked progression for the low spin spectrum with bands predicted in the near IR and to lower energies in the visible. Clearly the electronic spectrum matches the high spin state and provides additional confirmation for this assignment. For the strong field donors in **2**, one triarylphosphine and three thiolates, the stability of the  $S = 5/2$  state comes in part from the ligand enforced trigonal bipyramidal geometry.

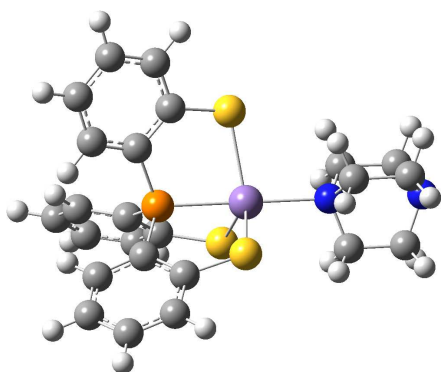


**Figure S19.** Optimized *ab initio* gas phase structure of the 3-protonated  $S = 5/2$  analog of the DABCO anion **2**. Density function theory, B3LYP/6-31+g\*, with a double zeta basis set used.

**Table S3.** Electronic Spectra Data Calculated with DFT-TD for **2** in nm (with intensity given as oscillator strength).

DFT-TD S=5/2	DFT-TD S=1/2	Experiment
	2358.29(0.0003)	
	1305.57(0.0002)	
	1151.95(0.0028)	
	941.48(0.0020)	
	801.80(0.0027)	
	636.10(0.0001)	
526.81(0.0068)	617.01(0.0002)	
526.28(0.0068)	526.22(0.0068)	535
486.62(0.0031)	493.06(0.0010)	
430.10(0.0008)	487.66(0.0005)	
429.95(0.0008)	479.10(0.0003)	
423.36(0.0004)	466.97(0.0022)	
411.52(0.0004)	456.57(0.0046)	
411.29(0.0004)	454.14(0.0002)	
408.78(0.0006)	452.28(0.0018)	
396.58(0.0013)	450.97(0.0046)	
395.71(0.0012)	443.18(0.0000)	
395.59(0.0012)	440.37(0.0004)	
386.74(0.0100)	432.96(0.0011)	
386.26(0.0000)	424.78(0.0095)	
386.14(0.0000)	423.22(0.0011)	
379.47(0.0000)	417.71(0.0011)	
378.85(0.0001)	406.75(0.0036)	

378.79(0.0001)		
373.87(0.0018)		
369.47(0.0034)		
369.46(0.0035)		
368.64(0.0107)		
367.77(0.0017)		
367.66(0.0017)		
366.05(0.0044)		
366.02(0.0044)		
365.44(0.0052)		370
363.00(0.0066)		
362.89(0.0066)		
361.19(0.0020)		

**Theoretical methods.** All of the calculations described above were performed using Gaussian 03.<sup>2</sup> Computations were carried out at the restricted Hartree-Fock (RHF),<sup>3</sup> and Density Functional Theory (DFT) levels. DFT calculations used the hybrid B3LYP functional and triple zeta 6-31+G\* basis sets.<sup>4</sup> The calculated molecular geometries were fully optimized and correspond to minima on the potential energy surface as confirmed by the absence of imaginary vibrational frequencies. All transition states were confirmed by reaction path (IRC) following calculations.

## References

1. Simulations of mass signals were examined by utilizing *IsoPro* 3.1 freeware.  
<https://sites.google.com/site/isoproms/>
2. Frisch, M. J.; Trucks, G. W.; Schlegel, H. B.; Scuseria, G. E.; Robb, M. A.;

- Cheeseman, J. R.; Zakrzewski, V. G.; Montgomery, J. A.; Stratmann, R. E.; Burant, J. C.; Dapprich, S.; Millam, J. M.; Daniels, A. D.; Kudin, K. N.; Strain, M. C.; Farkas, O.; Tomasi, J.; Barone, V.; Cossi, M.; Cammi, R.; Mennucci, B.; Pomelli, C.; Adamo, C.; Clifford, S.; Ochterski, J.; Petersson, J. A.; Ayala, P. Y.; Cui, Q.; Morokuma, K.; Malick, D. K.; Rabuck, A. D.; Raghavachari, K.; Foresman, J. B.; Cioslowski, J.; Ortiz, J. V.; Stefanov, B. B.; Liu, G.; Liashenko, A.; Piskorz, P.; Kamaromi, I.; Gomperts, R.; Martin, R. L.; Fox, D. J.; Keith, T.; Al-Laham, M. A.; Peng, C. Y.; Nanayakkara, A.; Gonzalez, C.; Challacombe, M.; Gill, P. M. W.; Johnson, B. G.; Chen, W.; Wong, M. W.; Andres, J. L.; Head-Gordon, M.; Replogle, E. S.; Pople, J. A. *Gaussian 98*, Gaussian Inc.: Pittsburgh, PA, **1998**.
3. Roothaan, C. C. New Developments in Molecular Orbital Theory. *J. Rev. Mod. Phys.* **1951**, *23*, 69-89.
  4. (a) Becke, A. D. Density-functional thermochemistry. III. The role of exact exchange. *J. Chem. Phys.* **1993**, *98*, 5648-5652; (b) Lee, C. Y., Yang, W. Parr, R. G. Development of the Colle-Salvetti correlation-energy formula into a functional of the electron density. *Phys. Rev. B* **1988**, *37*, 785-789.